A&A 494, 229–235 (2009)
DOI: 10.1051/0004-6361:200810228

Astronomy & Astrophysics

GRS 1915+105: high-energy insights with *SPI/INTEGRAL*

Spectral analysis of the Comptonized emission

R. Droulans and E. Jourdain

CESR – Universite de Toulouse (UPS), CNRS (UMR 5187), 9 Av. du Colonel Roche, 31028 Toulouse Cedex 4, France
e-mail: Robert.Droulans@cesr.fr

Received 20 May 2008 / Accepted 9 November 2008

ABSTRACT

Context. We report on results of nearly two years of INTEGRAL/SPI monitoring of the Galactic microquasar GRS 1915+105.
Aims. From September 2004 to May 2006, the source was observed twenty times with long (∼100 ks) exposures. We present an analysis of the SPI data and focus on the description of the high-energy (>20 keV) output of the source.
Methods. We performed temporal and spectral analysis of the SPI data and considered simultaneous 1.2–12 keV ASM data.
Results. We found that the 20–500 keV spectral emission of GRS 1915+105 was bound between two states. It seems that these high-energy states are not correlated with the temporal behavior of the source, suggesting that there is no direct link between the macroscopic characteristics of the coronal plasma and the variability of the accretion flow. All spectra are well-fitted by a thermal Comptonization component plus an extra high-energy power law. This confirms the presence of thermal and non-thermal electrons around the black hole.

Key words. radiation mechanisms: general – X-rays: individuals: GRS 1915+105 – accretion: accretion disks – gamma rays: observations

1. Introduction

GRS 1915+105 is among the most notorious accreting black holes in our Galaxy. Not only is it one of the brightest and most variable X-ray sources in the sky (see Castro-Tirado et al. 1992, for a first detection report; and Belloni et al. 2000, for detailed variability analysis), but it is also the first Galactic object in which superluminal plasma ejections have been observed (Mirabel & Rodriguez 1994). Consequently, much work has been done to try to understand the complex nature of the accretion flow (see e.g. the comprehensive analysis by Done et al. 2004) and the disk-jet coupling in this binary system. An extensive review of these aspects can be found in Fender & Belloni (2004). Very recently, Rodriguez et al. (2008a,b) have presented an extended report on GRS 1915+105 discussing insights gained from a 2-year monitoring campaign involving multi-wavelength observations.

However, most of the recent studies focus on the astonishing X-ray properties, the soft γ-ray emission (>100 keV) being generally observed at a poor signal-to-noise ratio. Understanding the high-energy behavior of the source is nevertheless very important, as it is assumed to trace the physical processes occurring in the innermost regions surrounding the black hole (e.g. Galeev et al. 1979; or Malzac 2007, for a review). Featuring good spectral resolution and sensitivity up to several MeV, SPI is a good instrument to tackle this issue.

The emission ranging from hundreds of eV up to almost 1 MeV is generally assumed to originate from two components (e.g. Vilhu et al. 2001). While the softer part is unanimously attributed to thermal emission from the disk, various interpretations exist concerning the origin of the high-energy emission. Detailed analysis of joint RXTE/OSSE observations allowed Zdziarski et al. (2001 and 2005) to rule out some of these interpretations. They suggest that the observed 10−500 keV emission originated from inverse Compton scattering of the soft disk photons by a hybrid thermal/non-thermal electron population.

In this paper we present all SPI observations of GRS 1915+105 from September 2004 to May 2006. We focus on gaining the most accurate high-energy picture of the source, mainly through extensive spectral analysis. First we briefly describe the instrument and our data reduction methods. The observational results are presented and discussed further in the concluding part of the paper.

2. Observations and data reduction

2.1. INTEGRAL/SPI

SPI is a high-resolution γ-ray spectrometer (Vedrenne et al. 2003) aboard the INTEGRAL observatory. The observational strategy of the INTEGRAL mission is based on approximately 3 day-long revolutions during which one or several fields of view are sampled by means of 30−40 min long fixed pointings, separated by a 2° angular distance. As the number of SPI pixels is small (among the initial 19 detectors, two broke down, reducing the detector plane to only 17 pixels), this so-called "dithering" scheme (see Jensen et al. 2003, for details) is essential for SPI image reconstruction. In particular, combining the data from a set of dithered pointings allows one to enhance the precision of flux extraction (see e.g. Joinet et al. 2005).

2.2. Data analysis

We analyzed all public data from nearly two years of SPI observations on GRS 1915+105 (September 2004−May 2006).

Table 1. Log of the SPI observations and basic source characteristics.

				SPI$_{22-50\ \mathrm{keV}}$		ASM$_{1.2-12\ \mathrm{keV}}$			
Obs ID	MJD start	MJD stop	Exp time (s)	$\langle F\rangle$(mCrab)	rms/$\langle F\rangle$(%)	$\langle F\rangle$(cts/cm^2/s)	rms/$\langle F\rangle$(%)	Γ	$\chi^2/27$
231	53 253.20	53 253.95	48 412.50	322.5 ± 5.0	20.2	51.9 ± 0.5	58.0	2.80 ± 0.06	0.97
242	53 285.10	53 285.75	42 782.20	259.5 ± 4.5	11.6	70.9 ± 0.7	8.20	3.09 ± 0.06	0.56
243	53 288.63	53 289.44	49 962.72	199.8 ± 4.4	16.0	62.1 ± 0.5	10.1	2.99 ± 0.10	1.08
246	53 296.35	53 297.53	77 174.90	305.8 ± 3.1	7.00	81.3 ± 0.3	28.2	3.02 ± 0.05	1.37
248	53 302.88	53 304.90	134 148.88	201.3 ± 2.7	18.5	69.4 ± 0.6	9.90	3.07 ± 0.07	0.84
250	53 309.14	53 310.22	72 648.77	199.1 ± 3.9	18.0	71.7 ± 0.4	9.00	3.10 ± 0.10	0.71
251	53 311.32	53 312.77	84 373.42	320.4 ± 3.9	16.7	53.3 ± 0.6	48.4	3.00 ± 0.06	1.12
255	53 324.27	53 325.46	81 422.62	152.1 ± 3.0	10.6	no data	no data	2.85 ± 0.09	0.64
295	53 442.95	53 444.15	85 681.48	255.5 ± 2.8	5.70	43.7 ± 0.4	5.10	3.47 ± 0.07	1.40
305	53 472.66	53 475.66	91 334.75	180.2 ± 2.7	11.8	no data	no data	3.52 ± 0.08	0.96
315	53 503.53	53 504.55	69 072.34	158.3 ± 3.4	20.7	134.1 ± 0.7	26.6	3.00 ± 0.10	1.26
361	53 640.92	53 641.58	70 136.04	123.2 ± 3.1	37.6	77.0 ± 0.7	35.7	3.24 ± 0.13	0.92
366	53 655.52	53 657.87	161 541.02	169.7 ± 3.0	19.7	59.1 ± 0.6	9.00	3.47 ± 0.09	1.46
367	53 659.23	53 660.83	109 687.94	160.4 ± 3.6	17.1	108.2 ± 0.5	40.9	3.48 ± 0.11	1.41
368	53 661.51	53 663.78	154 549.29	187.2 ± 2.8	18.6	113.7 ± 0.4	28.7	3.42 ± 0.07	1.68
369	53 664.31	53 665.53	52 753.31	194.0 ± 6.4	24.7	116.9 ± 0.6	43.5	3.43 ± 0.14	1.06
373	53 676.27	53 677.43	83 798.38	87.2 ± 3.8	36.6	77.6 ± 0.7	38.9	3.14 ± 0.18	1.07
379	53 694.27	53 695.47	90 421.32	183.1 ± 3.9	15.3	167.3 ± 1.5	32.6	3.08 ± 0.10	0.89
423	53 825.88	53 828.23	119 129.04	391.1 ± 4.2	7.90	29.1 ± 0.2	10.0	2.80 ± 0.04	3.07
431	53 851.94	53 852.20	15 509.04	278.7 ± 7.2	7.30	26.6 ± 0.4	7.20	2.80 ± 0.10	1.46

Notes: temporal behavior is parameterized in terms of average flux and fractional rms whereas the photon index Γ and χ^2/ν are the parameter and quality of a simple powerlaw model fit.

For each revolution, we first gathered all pointings where GRS 1915+105 was less than 12° off the central axis. Pointings showing contamination by solar flares or radiation belt exit/entry were excluded. The log of the resulting 1.7 Ms of observational coverage is given in Table 1. To detect the emitting sources in the field of view, we used the SPIROS software (Skinner & Connell 2003) to produce 20−50 keV images for each observation. The positions of the active sources (detected at a minimum of 5σ) were then given as input to a specific flux-extraction algorithm, using the SPI instrument response for sky-model fitting. From there we started to analyze the background and source behavior for each observation. We first allowed the background pattern, as well as the main source(s), to vary between successive pointings. In this way we determined each component's most appropriate variability timescale for the final data reduction. We used pointing durations (≈2 ks) as a timescale for the GRS 1915+105 light curves and adapted the time sampling for subsequent extraction of the 20 keV−8 MeV spectra according to the observed temporal behavior. This method allowed us to minimize the error bars without losing any scientific information.

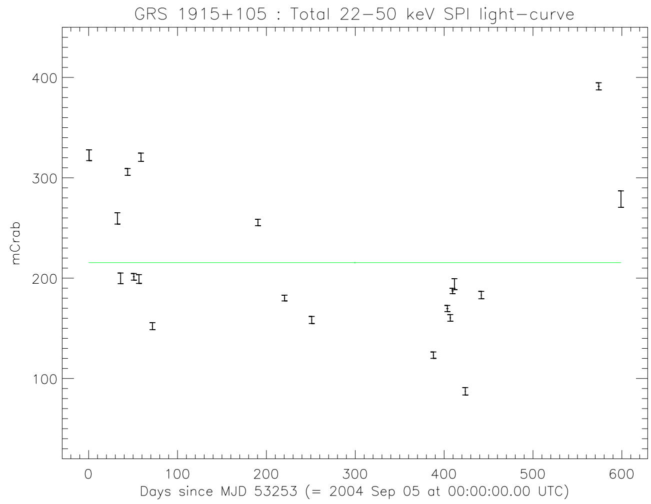

Fig. 1. Long-term variability of GRS 1915+105 in the SPI band. Each point represents the mean 20−50 keV flux per observation (corresponding to a time scale of about one day, see Table 1).

3. Results

3.1. Light curves

Figure 1 displays the total 20−50 keV light curve for our observational period. GRS 1915+105 shows relevant long-term variability, the averaged source flux per observation (≈one-day) spans between 90 and 380 mCrab, with an approximate uncertainty of 5 mCrab. On the shorter science-window time scale (≈2 ks), the obtained individual light curves generally show lower variability. Within a single observation, the source flux varies by at most a factor of 2. As GRS 1915+105 is well known for being very variable in X-rays, we also considered SPI-simultaneous 1.2−12 keV ASM light curves to compare the X- and soft γ-ray behavior of the source. We found an anti-correlation trend between the ~one-day averaged 1.2−12 and 20−50 keV source fluxes (Fig. 2) with a linear correlation factor ρ of −0.59 ± 0.02 and a 99% significance. On the science-window timescale, however, a positive flux-correlation is discernible for observation 368, as the source exhibits very strong variability (Fig. 5 right). The variability amplitudes (parameterized by fractional rms) are not straightforward for comparing since the time bins are very different between the two instruments. More importantly, the 1σ SPI errors for the individual light-curves have the same order of magnitude as absolute rms variability, thus limiting any solid scientific interpretation.

3.1.1. Spectral analysis

We used XSPEC 11.3.2 (Arnaud 1996) for spectral analysis. First, each observation-averaged spectrum was fitted with a basic powerlaw model which gives a good description of most of the data. Then we characterized the spectra by 20−50 keV flux

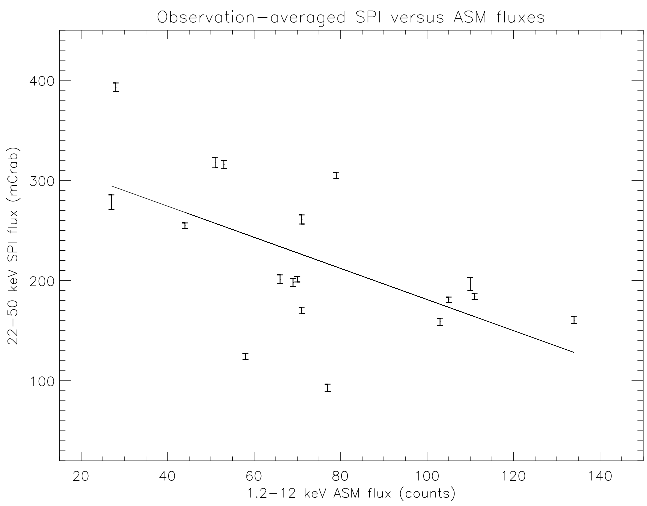

Fig. 2. One-day time scale flux-flux relation between the 1.2−12 and 20−50 keV bands. We observe an anticorrelation in the flux trend between the two bands.

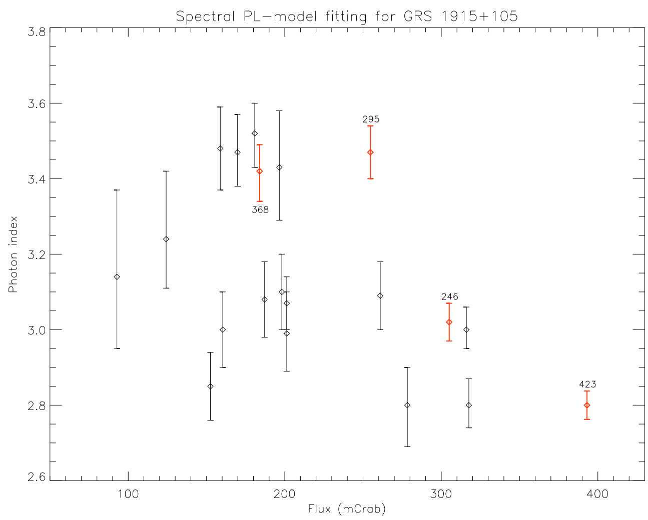

Fig. 3. Basic source characteristics: model photon index versus mean flux per observation. The observations that are discussed in the text are highlighted in red.

and best-fit photon index, the latter being found to range from 2.8 to 3.5, with a typical uncertainty of 0.1. The results are summarized in Table 1 and illustrated by a photon index versus flux diagram given in Fig. 3. We used this figure to select four observations that will be presented in more detail in the following sections. We selected the observations made during INTEGRAL revolutions 295 and 423 since they both have rather high average fluxes (and therefore good signal-to-noise ratios), but at the same time very different spectral shapes. Furthermore, the light-curves showed no significant variability during these observations (neither in the 20−50 keV band nor in X-rays), hence allowing a meaningful analysis of the observation-averaged spectrum. In addition, we selected two other observations (Rev. 246 and 368) because they were part of large multi-wavelength campaigns, allowing us to put the SPI data in a broader context.

3.1.2. Observations 295 and 423

From the ASM light-curves in Fig. 4, we see that during both observations GRS 1915+105 showed very similar X-ray activity, characterized by low flux and almost no variability. The temporal properties in the 20−50 keV band are also quite similar, with again little variability during both observations. On the other hand, spectral characteristics are found to be significantly different, with photon indices of 3.47 ± 0.07 and 2.80 ± 0.04 respectively. We then investigated these differences through more detailed spectral modeling. From Table 1 one can see that the simple power law model gives a rather poor fit for observation 295. More precisely, we noticed that above 100 keV all spectral points are located above the fitted power law. Pure thermal Comptonization models like COMPTT (where the Comptonized spectrum is completely determined by the plasma temperature and its optical depth, Titarchuk 1994) can thus be ruled out (χ^2/ν = 72/26, see Table 2). Assuming that the low-energy part is nonetheless produced through thermal Comptonization, one needs to add another spectral component. We thus chose to add a power law as a phenomenological description of the observed high-energy tail. Given the error amplitude above 100 keV, we arbitrarily fixed the photon index to 2.0. The resulting fit ($kT_e = 16.3^{+1.2}_{-0.9}$ keV and $\tau = 0.57$[1]) agrees very well with our data (χ^2/ν = 17/25) and the *F-TEST* indicates a probability of $\approx 10^{-9}$ that this improvement has been a chance event. As a last step we applied the Poutanen & Svensson (1996) COMPPS model that describes Comptonization from a hybrid thermal/non-thermal electron plasma. This iterative scattering method assumes a power law distribution ($\propto \gamma^{-\Gamma_e}$) up to a Lorentz factor γ_{min} below which the plasma thermalizes to a Maxwellian distribution. We fixed a spherical geometry and assumed the reflection component to be insignificant, enabling a straightforward comparison with COMPTT+PL. Note that COMPPS poses more constraints than COMPTT+PL, as it requires both components (thermal and non-thermal) to be linked, whereas the former does not. Equally good fitting results (χ^2/ν = 17/25) for both models indicate that the observed 20−500 keV emission is most likely to originate from thermal and non-thermal Comptonization processes.

For observation 423, the basic powerlaw fit is clearly unacceptable (χ^2/ν = 83/27) due to the marked curvature around 50 keV, leaving clear evidence of thermal processes. Replacing the power law by a pure thermal component improved the fit and gave χ^2/ν = 42/26. However, this interpretation is not able to account for the observed emission above 200 keV, again suggesting the presence of an additional component. We thus keep the hybrid Comptonization models (χ^2/ν = 37/25 for COMPTT+PL and χ^2/ν = 37/24 for COMPPS) as our preferred description for observation 423.

All fitting results are summarized in Table 2 and discussed in Sect. 4.

3.2. Observations 246 and 368

Both observations have already been studied intensively. Observation 246 is discussed by Rodriguez et al. (2008b), who conducted detailed spectro-temporal analysis by means of multi-wavelength coverage. They found that the source showed periodic X-ray cycles, identified as alternations of ν and ρ classes (see Belloni et al. 2000, for definitions). INTEGRAL observation 368 was again part of a large multi-wavelength campaign, this time involving the Suzaku satellite (Ueda et al. 2006). These authors identified the observed X-ray variability pattern to be the signature of a high flux transition from

[1] Fixed to its best-fit value for error calculation on kT_e.

Table 2. Spectral fitting results for the high-lighted observations.

		COMPTT / COMPPS				PL				
Obs ID	kT_{bb} (keV)	kT_{e} (keV)	τ	$\gamma_{\min}$	Γ_{e}	F_{comptt}	α	K_{pl}	χ^2/ν	FTEST
		$83^{+4.2}_{-2.3}$	0.08	–	–	–	–	–	32/26	
246	1.0f	$18.2^{+1.1}_{-1.0}$	0.97	–	–	$3.64^{+0.04}_{-0.04}$	2.0f	$3.48^{+1.05}_{-0.96}$	27/25	4×10^{-2}
		$16.20^{+0.31}_{-0.26}$	$3.68^{+0.23}_{-0.20}$	1.36	2.12	–	–	–	28/24	
		44	0.18	–	–	–	–	–	72/26	
295	1.5f	$16.3^{+1.2}_{-0.9}$	0.57	–	–	$2.73^{+0.03}_{-0.03}$	2.0f	$3.95^{+0.66}_{-0.56}$	17/25	2×10^{-9}
		$14.43^{+0.23}_{-0.23}$	$2.70^{+0.12}_{-0.17}$	1.30	2.36	–	–	–	17/24	
		39	0.20	–	–	–	–	–	74/26	
368	1.5f	$13.4^{+1.0}_{-0.9}$	0.86	–	–	$1.94^{+0.03}_{-0.03}$	2.0f	$3.28^{+0.54}_{-0.56}$	29/25	1×10^{-6}
		$15.10^{+0.27}_{-0.29}$	$2.64^{+0.21}_{-0.20}$	1.31	2.35	–	–	–	29/24	
		$41^{+1.2}_{-1.7}$	0.45	–	–	–	–	–	42/26	
423	1.0f	$19.2^{+1.0}_{-1.0}$	1.20	–	–	$4.91^{+0.05}_{-0.05}$	2.0f	$4.27^{+1.29}_{-1.38}$	37/25	8×10^{-2}
		$17.54^{+0.31}_{-0.28}$	$4.40^{+0.20}_{-0.20}$	1.38	2.11	–	–	–	37/24	
		48	0.13	–	–	–	–	–	152/26	
SS	1.5f	$16.5^{+0.6}_{-0.6}$	0.62	–	–	$2.07^{+0.03}_{-0.03}$	2.0f	$2.75^{+0.28}_{-0.29}$	31/25	3×10^{-10}
		$14.72^{+0.16}_{-0.13}$	$2.70^{+0.10}_{-0.25}$	1.31	2.35	–	–	–	31/24	
		$38^{+0.9}_{-0.9}$	0.47	–	–	–	–	–	30/26	
HS	1.0f	$17.7^{+0.7}_{-0.7}$	1.28	–	–	$4.13^{+0.04}_{-0.04}$	2.0f	$3.31^{+0.91}_{-0.95}$	19/25	8×10^{-4}
		$18.14^{+0.31}_{-0.37}$	$4.02^{+0.15}_{-0.14}$	1.39	2.21	–	–	–	19/24	

Notes: for each spectrum, the first row corresponds to a simple thermal comptonization model (COMPTT), the second row contains the COMPTT + PL parameters and the last gives the variables of the COMPPS model. The seed photon temperature is fixed to 1.0 keV and 1.5 keV for the harder and softer spectra respectively. COMPTT errors are calculated on kT_{e} while fixing τ to its best fit value. For the COMPPS model, the geometry parameter is fixed to zero (spherical) and neither reflection nor ionization is taken into account. The error bars are simultaneously evaluated on kT_{e} and τ while we fixed $\gamma_{\min}$ and Γ_{e} to their best fit values. F_{comptt} denotes the integrated 20–500 keV energy flux from the thermal component and is given in units of $\times10^{-9}$ erg/cm^2/s. K_{pl} is the flux normalization at 100 keV of the non-thermal power law and is given in units of $\times10^{-5}$ photons cm^{-2} s^{-1} keV^{-1}.

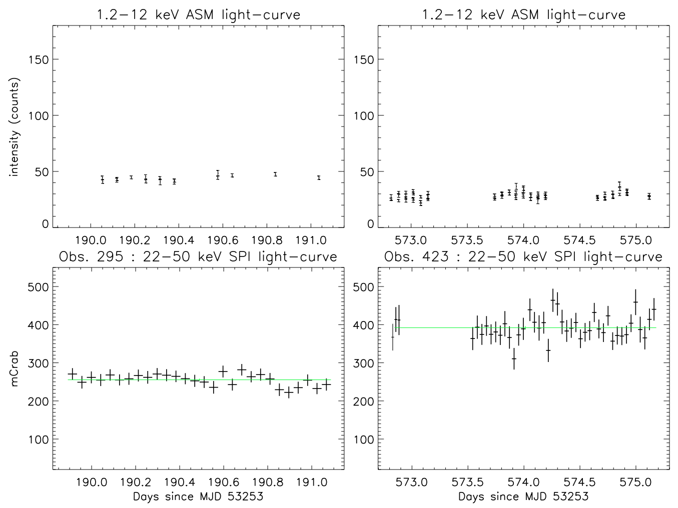

Fig. 4. ASM and SPI light curves for observations 295 and 423. For both observations the source exhibits low flux and very little variability in the ASM band. In the 20−50 keV SPI band, we observe similar stability on the science-window timescale with intermediate and high average flux, respectively.

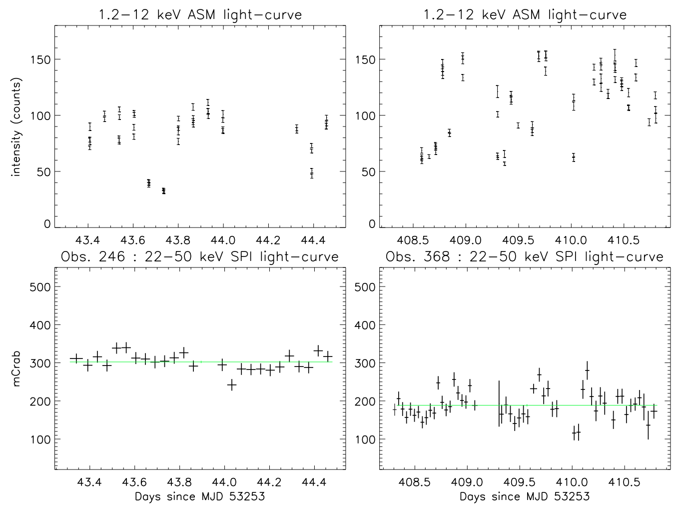

Fig. 5. ASM and SPI light curves for observations 246 and 368. During the latter a correlation (on the ≈2 ks science-window time scale) between the 1.2−12 and 20−50 keV bands is noticeable, hinting that both bands are tracing the evolution of the Comptonized emission.

a soft class χ to class θ. We find the same variability pattern in X-rays as in the 20−50 keV SPI band (Fig. 5), indicating that both bands probably sample the temporal behavior of the same component. For observation 246 there seems to be a similar correspondence, although less clear due to lower variability amplitude in the SPI band. Both spectra are fitted with thermal + non-thermal Comptonization models (COMPTT+PL and COMPPS), which provide the best agreement to the data (see Table 2). Compared to the joint JEMX/ISGRI spectrum from observation 246 (Rodriguez et al. 2008b), our SPI data are found to almost have the same spectrum than the one produced by these authors from only stable low/hard X-ray intervals (Interval I in Rodriguez et al. 2008b), whereas the very short X-ray spikes originating from the disk (Intervals II and IV) are washed out. This shows that the SPI spectra of the one day averaged Comptonized emission are not influenced by any peculiar outburst-behavior on very short time scales. Likewise,

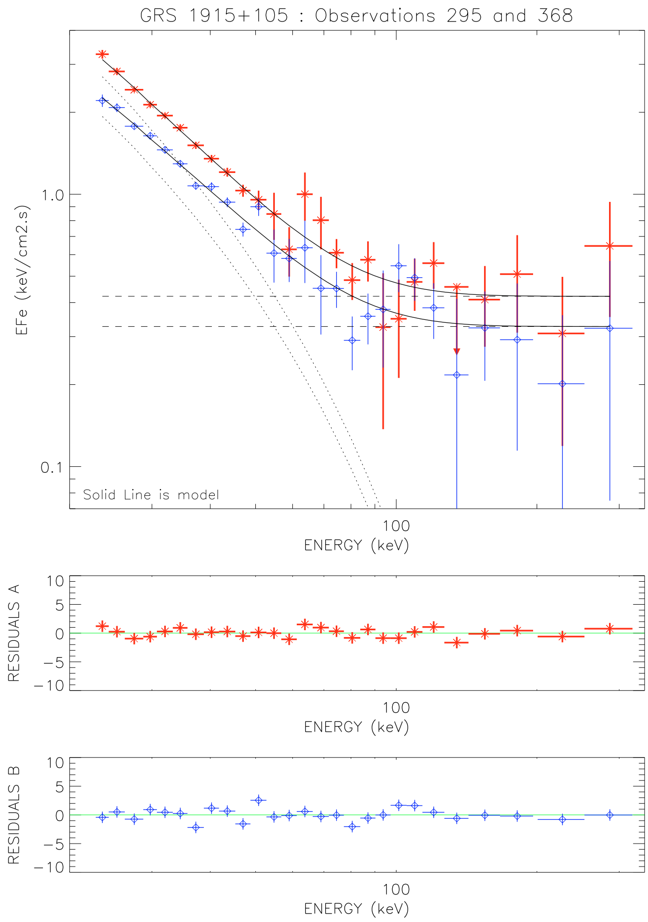

Fig. 6. COMPTT+PL best fits for observations 295 (red stars) and 368 (blue diamonds). Both observations have very similar spectral shapes.

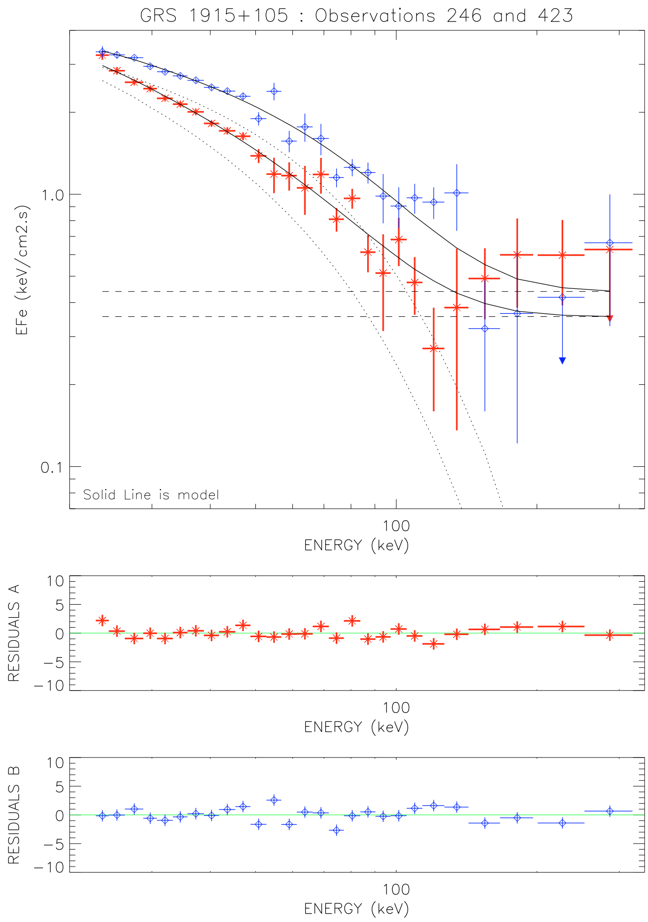

Fig. 7. COMPTT+PL best fits for observations 246 (red stars) and 423 (blue diamonds).

a comparison with simultaneous Suzaku observations leads to similar conclusions for observation 368.

3.3. Cross-comparison

When comparing the results of these four high-lighted observations, we notice that the X-ray variability and the spectral behavior at higher energies (>20 keV) seem to be completely uncorrelated. Except for a slight difference in flux, the SPI spectra from observations 368 and 295 (illustrated in Fig. 6) show the same characteristics, whereas the temporal behavior in X-rays is seen to be dramatically different (compare Figs. 4 left and 5 right). A similar high-energy correspondence can be observed between observations 246 and 423 (Fig. 7), although again no similarities are found in X-rays. We thus see that for similar X-ray variability, the 20−500 keV spectra can be different and reciprocally that for similar (~one day averaged) high-energy spectral behavior, the source may exhibit very unlike 1.2−12 keV activity.

3.4. Composite spectra

For further investigation of the high-energy tail of GRS 1915+105, we decided to group data from observations with similar spectra. Improved statistics should allow us to put better constraints on the parameters of the fitted models. Hence, we isolated two opposite groups in the spectral index versus flux diagram (Fig. 3) for which we generated composite spectra. The first group is characterized by a rather low 20−50 keV flux (≈200 mCrab) and a very soft spectral shape ($\Gamma \approx 3.45$); hereafter we will call it the *soft sample*. The second group, on the other hand, has hard colors ($\Gamma \approx 2.90$) and high average flux (≈330 mCrab) in the 20−50 keV band, so it is called the *hard sample*. We note that the previously presented observations 295/368 and 246/423 are representative of each group, respectively. As some observations had intermediate characteristics, we excluded them from the regrouped spectra to avoid mixing different high-energy patterns. As a result, our two samples are likely to describe the boundary Comptonization states between which the source seems to be continuously switching.

We fitted both composite spectra shown in Fig. 8 with several models and summarize the results in Table 2. Each time the thermal + non-thermal Comptonization models gave the best fit to the data and demonstrated the need for an additional high-energy component (see *F-TEST* values in Table 2). The composite spectral analysis thus confirms the previously outlined interpretation, which will be further discussed in the next section.

4. Discussion

We interpret the 20−500 keV emission of GRS 1915+105 as a combination of thermal and non-thermal Comptonization. Given the similarities of the observed temporal properties, the ASM band is likely to sample the same emission component as the 20−50 keV SPI band. This agrees with the results of Done et al. (2004), who show that except for ultrashort disc-dominated

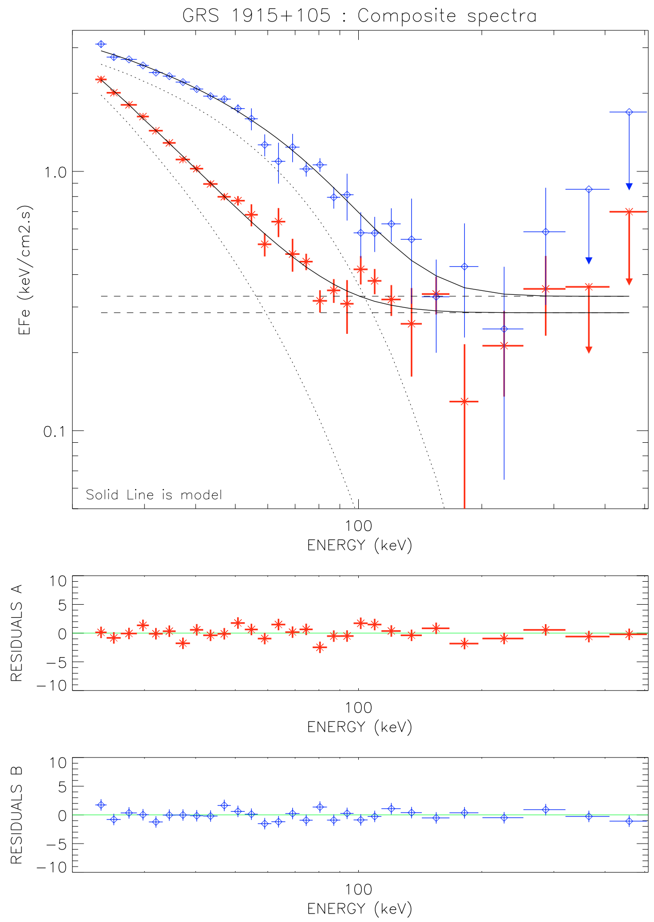

Fig. 8. COMPTT+PL best fits for the composite spectra, plotted in red stars and blue diamonds for the soft and hard samples, respectively. These spectra illustrate the boundary characteristics of the one-day averaged high-energy emission of GRS 1915+105.

X-ray spikes the accretion diskc has no significant effect above 3 keV (see also Rodriguez et al. 2008b). The spectra obtained during observations 295 and 368 show that for different X-ray classes (i.e. different temporal behavior of the accretion flow) the high-energy spectra can be very similar. Conversely, observations 295 and 423 show that, within stable emission episodes, there can be significant differences in the spectral behavior of the source. Assuming that the 3−50 keV emission originates from the Comptonizing corona (see Malzac 2007; or Done et al. 2007, for details), this clearly indicates that there is no correlation between the temporal variability and the macroscopic properties of the Comptonizing flow. As they give better statistics above 100 keV, we use our composite spectra to further discuss both Comptonization components and put our findings in a more general context.

4.1. The soft sample

From spectral modeling we find the intersection point of the two components to be around 60 keV. At higher energies, the non-thermal processes dominate. Both the thermal and non-thermal components have approximately the same luminosity above 20 keV. If these two components originate from the same population (COMPPS results), the electrons are found to thermalize around Lorentz factor $\gamma_{\min} \approx 1.30$. The mildly hot Compton cloud ($kT_e = 14.72 \pm 0.15$ keV) is found to be marginally optically thick ($\tau = 2.7^{+0.10}_{-0.25}$), which is the expected configuration for black-hole binaries in the very high state (Done & Kubota 2006). We suggest that our soft composite spectrum gives a canonical high-energy representation of GRS 1915+105 in low coronal luminosity states.

4.2. The hard sample

Concerning the hard sample, the luminosity of the non-thermal component is found to be roughly the same (compatible within the uncertainties) as for the previously discussed soft sample; however, the intersection point of the two components is now around 110 keV (which corresponds to a Lorentz factor $\gamma_{\min} \approx 1.39$), showing that the main difference lies in the properties of the Comptonizing thermal electrons of the corona. The plasma is found to be either hotter for similar optical depths or optically thicker for similar electron temperatures (or a mixture of both), thus enhancing the higher observed 20−50 keV flux. Even though this situation cannot be completely resolved due to the observational $kT - \tau$ degeneracy, spectral fits with COMPPS indicate that it is likely that there has been a significant increase in opacity, whereas electron temperature remains around 15−20 keV. In either case, this does not affect the estimation of the total 20−500 keV luminosity issued from thermal Compton scattering, which is found to be enhanced by a factor of 2 ± 0.04 in comparison with the soft sample. We interpret our spectrum as a typical representation for the high-energy emission of GRS 1915+105 in high coronal luminosity states.

5. Summary and conclusions

We conducted detailed high-energy spectral analysis of the microquasar GRS 1915+105 using all available SPI data from September 2004 to May 2006, and presented our observational results on the source's high-energy output. We can summarize our findings as follows.

We found that the ~one-day averaged 20−500 keV spectral emission is always between two boundary states, *hard* and *soft*, which we illustrated through spectral modeling. We confirm that in the INTEGRAL-SPI data we observe no high-energy cutoff for GRS 1915+105 (Fuchs et al. 2003; Rodriguez et al. 2008b). We suggest that the high-energy cutoff from thermal Comptonization is drowned out by an additional non-thermal component. We found the non-thermal component to be statistically required in both composite samples. The spectral differences we observed in hard X-rays (20−50 keV) are most likely to be coupled to the evolution of the thermal electron plasma. The bolometric luminosity calculated from the thermal component varies by a factor of 2 between soft and hard samples. In contrast, the obtained fits indicate that the non-thermal component is fairly stable. This implies that both components are not necessarily linked; i.e. they could originate from dissociated electron populations. Hence as suggested by Rodriguez et al. (2008b), the non-thermal component might be from emission from the jet. Given the length of the high-energy observations (SPI ≈ 3 days or OSSE ≈ 15 days), it is difficult to investigate the connection between the various X-ray classes and the high-energy spectra. We pointed out that there is no direct correlation between the observed X-ray variability patterns and the 20−500 keV SPI spectra. This shows that the macroscopic properties of the Comptonizing thermal electrons evolve independently from the fluctuations of the accretion flow. These aspects will be adressed in a subsequent paper using multiwavelength coverage. In summary, our results give a recent high-energy picture of GRS 1915+105 and once more underline the complex nature of the accretion processes operating around this archetypal microquasar.

Acknowledgements. The SPI project has been completed under the responsibility and leadership of the CNES. We are grateful to the ASI, CEA, DLR, ESA, INTA, NASA, and OSTC for support. Specific software packages used for this work have been developed by E. Durand at the CESR, Toulouse. We are grateful to the anonymous referee for the fruitful comments that allowed us to improve the quality of this paper.

References

Arnaud, K. A. 1996, in Astronomical Data Analysis Software and Systems V, ed. G. H. Jacoby, & J. Barnes, San Francisco, Astron. Soc. Pac., ASP Conf. Ser., 101, 17
Belloni, T., Klein-Wolt, M., Méndez, M., et al. 2000, A&A, 355, 271
Castro-Tirado, A. J., Brandt, S., & Lund, N. 1992, IAUC, 5590, 2
Done, C., & Kubota, A. 2006, MNRAS, 371, 1216
Done, C., Wardziński, G., & Gierliński, M. 2004, MNRAS, 349, 393
Done, C., Gierliński, M., & Kubota, A. 2007, A&AR, 15, 1
Fender, R. P., & Belloni, T. 2004, ARA&A, 42, 317
Fuchs, Y., Rodriguez, J., Mirabel, F., et al. 2003, A&A, 409, L35
Galeev, A. A., Rosner, R., & Vaiana, G. S. 1979, ApJ, 229, 318G
Jensen, P. L., Clausen, K., Cassi, C., et al. 2003, A&A, 411, L7
Joinet, A., Jourdain, E., Malzac, J., et al. 2005, ApJ, 629, 1008
Malzac, J. 2007, ApJS, 170, 175
Mirabel, I. F., & Rodríguez, L. F. 1994, Nature, 371, 46
Poutanen, J., & Svensson, R. 1996, ApJ, 470, 249
Rodriguez, J., Shaw, S. E., Hannikainen, D. C., et al. 2008a, ApJ, 675, 1436
Rodriguez, J., Shaw, S. E., Hannikainen, D. C., et al. 2008b, ApJ, 675, 1449
Skinner, G., & Connell, P. 2003, A&A, 411, L123
Titarchuk, L. 1994, ApJ, 434, 313
Ueda, Y., Ishioka, R., Sekiguchi, K., et al. 2006, in Proceedings of the VI Microquasar Workshop: Microquasars and Beyond PoS(MQW6), 023
Vedrenne, G., Roques, J. P., Schönfelder, V., et al. 2003, A&A, 411, L63
Vilhu, O., Poutanen, J., Nikula, P., & Nevalainen, J. 2001, ApJ, 553, L51
Zdziarski, A. A., Grove, J. E., Poutanen, J., et al. 2000, ApJ, 554, L45
Zdziarski, A. A., Gierliński, M., Rao, A. R., et al. 2005, MNRAS, 360, 825